Modeling gas flow in low-permeability formations: an efficient combination of mixed finite elements and high order time integration schemes

Anis A. Younes, Lingai Guo, François Lehmann, Marwan Fahs, Hussein Hoteit

Modeling gas flow in low-permeability formations: an efficient combination of mixed finite elements and high order time integration schemes

Anis Younes[a,*], Lingai Guo[a,b], François Lehmann[a], Marwan Fahs[a], Hussein Hoteit[b]

[a] *Institut Terre et Environnement de Strasbourg, Université de Strasbourg, CNRS, ENGEES, UMR 7063, 5 rue René Descartes 67084 Strasbourg, France*

[b] *Physical Science and Engineering Division, King Abdullah University of Science and Technology, Thuwal, Saudi Arabia*

Submitted to *Computers & Fluids*

Corresponding author: Anis Younes

E-mail: younes@unistra.fr

Abstract

Numerical simulation of gas flow in low permeability formations is a challenging task due to the high nonlinearity induced by (*i*) the compressibility of the gas, (*ii*) the Klinkenberg slippage effect and (*iii*) the Langmuir adsorption of the gas on the pore surface. Because of these nonlinearities, modeling gas flow in low permeability formations requires a great deal of computational effort. In this work, we develop an efficient numerical model using advanced spatial and temporal discretization methods for a simultaneous solution of the coupled equations of gas flow, cubic Peng-Robinson equation of state, slippage effect and Langmuir adsorption.

The spatial discretization is performed with the lumped hybrid formulation of the mixed finite element method which is well adapted for fluid flow in heterogeneous porous media. The time integration is performed with high-order methods via the method of lines (MOL) which allows large time steps and efficient solution of the nonlinear system of equations.

Numerical experiments, performed for gas extraction in a heterogeneous domain, point out the high efficiency of the new model since it can be until 10 times more efficient than the classical first-order time discretization method. Results of global sensitivity analysis show that the intrinsic gas-phase permeability and the Klinkenberg factor are the most influential parameters controlling the pumping rate in the case of gas extraction in a homogeneous domain.

Keywords:

Gas flow, Klinkenberg slippage effect, Langmuir adsorption, Mixed Finite Element, Method of Lines, Global sensitivity analysis.

1. Introduction

Gas flow in porous media can be encountered in several areas such as, natural gas engineering, CO_2 sequestration in subsurface reservoirs, contaminant transport and remediation, as in the case of vapor extraction to clean up contamination in shallow aquifers (Baehr and Hult, 1991; Essaid et al., 2015; Hughes et al., 2012). For all these areas, numerical models are powerful tools for understanding and optimizing studies of gas flow in porous media.

Numerical simulation of gas flow in low permeability formations is more complex than liquid flow (Jia et al., 2017; Shabro et al., 2011). The complexity is mainly related to the nonlinearity induced by (*i*) the high compressibility of the gas, (*ii*) the slippage effect and (*iii*) the adsorption of the gas on the pore surface. The first nonlinearity is related to the compressibility of the gas which often needs to be calculated by solving the cubic Peng-Robinson (Peng and Robinson, 1976) equation of state (EOS), in which the coefficients are dependent on the gas pressure. Thus, due to the compressibility of the gas, the fluid flow equation and the EOS of gas are coupled and have to be solved simultaneously, which induces a strong nonlinearity and requires excessive computational time. The second nonlinearity is related to the non-Darcy Klinkenberg (1941) effect which represents the slippage effect in low-permeability formations. This phenomenon occurs because in micro and nano pores, the no-slip surface condition may not be satisfied. The Klinkenberg effect is the origin of a nonlinear dependence of the effective permeability on the gas pressure and can have a significant impact on the gas flow behavior. Finally, the last nonlinearity is related to the adsorption of the gas on the pore surface which is often described by the nonlinear Langmuir isotherm model.

Due to these nonlinearities, modeling gas flow in low permeability formations is a difficult task that often requires high computational cost. Several techniques have been developed to improve the efficiency of the numerical solution of fluid flow in porous media such as domain decomposition (Wang et al., 2005), parallel computing (Wu et al., 2002) or multigrid methods (Bastian and Helmig, 1999). Various numerical models (El Amin et al., 2018, 2017; Huyakorn et al., 1994; Li et al., 2020; Pruess, 1991; Salama et al., 2017; Samuel and Muggeridge, 2020; Shabro et al., 2011; Wilson et al., 1987; Xiao et al., 2017) have been developed for gas flow in porous media. Some specific techniques have been proposed to reduce the computational burden associated with the solution of the gas flow equation in low permeability formations. For instance, Li et al. (2020) proposed to replace the original model with a surrogate one that uses a low dimensional space with small degrees of freedom (DOF). The surrogate model allows a substantial reduction of the computational cost, however, the accuracy and efficiency of the solution is highly sensitive to the selection of the modes in the surrogate model (Li et al., 2020). El Amin et al. (2018) used a semi-implicit scheme for the time discretization with the Mixed Finite Element (MFE) method for the simulation of gas flow in tight geological media. The semi-implicit numerical scheme keeps all nonlinear terms at the old time level and, as a consequence, the nonlinearity is removed and no Newton iterations are required. However, although convenient, it is known that semi-implicit numerical schemes can suffer from loss of accuracy and stability constraints for highly nonlinear problems.

In this work we develop an efficient model based on advanced spatial and temporal discretization methods for a simultaneous solution of the coupled equations of gas flow and EOS with nonlinear slippage and adsorption. The spatial discretization is performed with the lumped formulation of the MFE method on general triangular meshes. Further, to reduce the

97 computational burden of the solution of the nonlinear system of equations, the time
98 integration is performed with high-order methods via the method of lines (MOL).
99 The Mixed Finite Element (MFE) method (Brezzi and Fortin, 1991; Chavent and Jaffré, 1986;
100 Younes et al., 2010) is well adapted for solving elliptic diffusion problems. The method
101 ensures local mass conservation and can easily handle heterogeneous domains with
102 discontinuous parameter distributions and unstructured meshes. The hybridization technique
103 yields a final system with a reduced number of unknowns and a symmetric positive definite
104 system matrix (Chavent and Roberts, 1991). A lumped formulation of the hybrid-MFE
105 method was developed by Younes et al. (2006) and allows: (*i*) to improve the monotonous
106 character of the hybrid-MFE solution (Koohbor et al., 2020; Younes et al., 2006) and (*ii*)
107 unlike the standard method, it keeps the time derivative continuous which allows employment
108 of high-order time integration methods. Thus, sophisticated ODE solvers, where the order of
109 the time integration as well as the time step size are optimized during the simulation, can be
110 employed. Notably, the DASPK time solver (Brown et al., 1994) was shown to be very
111 efficient in solving saturated and unsaturated fluid flow and mass transport equations in
112 heterogeneous porous media (Younes et al., 2022, 2011, 2009). This solver is employed here
113 to solve the fully coupled nonlinear system of equations of gas flow and Peng-Robinson EOS
114 with slippage effect and nonlinear adsorption.
115 The article is structured as follows. In section 2, we recall the mathematical model governing
116 gas flow in low permeability formations. In section 3, we develop the spatial discretization
117 based on the lumped-MFE method that we combine with high-order time integration methods.
118 In section 4, numerical experiments are performed to investigate the efficiency of the new
119 model. Section 5 concludes the study and reviews the main findings.

2. The mathematical model for gas flow in low-permeability media

The mass conservation of gas transport through low-permeability formations, taking into account the loss of mass of gas per adsorption is:

$$\frac{\partial(\rho\phi)}{\partial t}+\frac{\partial\left[(1-\phi)q_{ad}\right]}{\partial t}+\nabla.(\rho\boldsymbol{u})=Q_s \tag{1}$$

where ρ is the gas density (kg/m^3), ϕ (-) porosity, q_{ad} the mass of gas adsorbed per solid volume of rock (kg/m^3), $\boldsymbol{u}$ (m/s) the Darcy velocity of gas and Q_s the external sink/source term (kg/m^3/s).

Gas flows in porous media differently from liquid. As gas is transported through small pores, some of the gas adheres (clings) to pore surfaces due to the diffusion of gas molecules. The most common adsorption model used to estimate the amount of adsorbed gas is based on the Langmuir isotherm (Civan et al., 2011; Cui et al., 2009; Foo and Hameed, 2010) :

$$q_{ad}=\frac{\rho_s M_g}{V_{std}}\frac{V_L p}{p_L+p} \tag{2}$$

where ρ_s (kg/m^3) denotes the material density of the porous sample, V_L (m^3/kg) is the Langmuir gas volume, V_{std} (m^3/mol) is the molar volume of gas at standard temperature (273.15 K) and pressure (101325 Pa), p (Pa) is the gas pressure, p_L (Pa) is the Langmuir gas pressure and M_g (kg/mol) is the molecular weight of gas.

The gas density ρ (kg/m^3) is given by the real-gas equation of state as:

$$\rho=\frac{M_g}{R_g T}\frac{p}{Z} \tag{3}$$

where Z (-) is the real gas deviation factor also named Z-factor, T (K) is temperature (considered constant in this work), and R_g is the universal gas constant (8314 J/kmol/K).

Several methods can be used to calculate the Z-factor, such as empirical correlations (Mahmoud, 2014; Wang et al., 2023), neural networks (Baniasadi et al., 2012), genetic algorithms and optimization methods (Chamkalani et al., 2013), molecular dynamics simulations (Moiseeva and Malyshev, 2019) or by solving the implicit EOS.

Empirical correlations are the easier and faster methods but are usually developed using specific data set and are therefore not accurate. The EOS is the most accurate method but is difficult to solve because of its highly nonlinearity. There are several EOS in the literature, among them the Var der Waals EOS, the Redlich-Kwong EOS, and the Peng-Robinson EOS. In this work, we choose the Peng-Robinson EOS since it is one of the most useful and successfully applied models in petroleum engineering (Lopez-Echeverry et al., 2017).

The cubic implicit Peng-Robinson EOS can be expressed as follows (Elliott and Lira, 2012):

$$Z^3 - (1-B)Z^2 + \left(A - 2B - 3B^2\right)Z - \left(AB - B^2 - B^3\right) = 0 \tag{4}$$

where

$$A \approx 0.45724\left(1+\kappa\left(1-T_r^{0.5}\right)\right)^2 \frac{p_r}{T_r^2} \text{ and } B \approx 0.0778\frac{p_r}{T_r} \tag{5}$$

with

$$\kappa \approx 0.37464 + 1.54226\omega - 0.26992\omega^2 \tag{6}$$

where, ω is the acentric factor (-), $p_r = p/p_c$ and $T_r = T/T_c$ are reduced pressure (-) and reduced temperature (-), respectively, with p_c and T_c the critical pressure (Pa) and the critical temperature (K), respectively.

Neglecting the compressibility of the porous medium as compared to that of the gas, Eq. (1) writes:

$$\phi\frac{\partial\rho}{\partial p}\frac{\partial p}{\partial t} + (1-\phi)\frac{\partial q_{ad}}{\partial p}\frac{\partial p}{\partial t} + \nabla.(\rho\boldsymbol{u}) = Q_s \tag{7}$$

Using Eq. (2) and Eq (3), we obtain

$$\begin{aligned}\frac{\partial\rho}{\partial p} &= \frac{M_g}{R_g T Z}\left(1 - \frac{\partial Z}{\partial p}\frac{p}{Z}\right)\\ \frac{\partial q_{ad}}{\partial p} &= \frac{\rho_s M_g}{V_{std}}\frac{V_L p_L}{\left(p_L + p\right)^2}\end{aligned} \tag{8}$$

Neglecting gravity, the conservation of momentum of gas flowing through the porous medium writes:

$$\boldsymbol{u} = -\frac{k}{\mu}\nabla p \tag{9}$$

where μ ($\mathrm{Pa \cdot s}$) denotes the dynamic viscosity of the flowing gas and k ($\mathrm{m^2}$) the effective permeability.

In low permeability formations, the gas permeability is enhanced by 'slip flow' due to molecular collusions with the pore wall rather than with other gas molecules (Wu et al., 1998). This effect, named Klinkenberg gas slippage effect, may have a significant impact on gas flow behavior, especially in low permeability formations (Reda, 1987). According to Klinkenberg (1941), the effective gas permeability at a finite pressure is given by

$$k = k_0\left(1+\frac{\beta}{p}\right) \tag{10}$$

where k_0 ($\mathrm{m^2}$) is the absolute gas-phase permeability under very large gas-phase pressure, also called intrinsic permeability, and β (Pa) is the Klinkenberg factor. This factor depends on the pore structure of the medium and the temperature for a given gas. Jones (1972) found that β generally decreases with increasing permeability.

Combining Eq. (9) and Eq. (10) with Eq. (3) gives:

$$\boldsymbol{q} = \rho\boldsymbol{u} = -K\nabla p \tag{11}$$

where

$$K = \frac{M_g}{\mu R_g T}k_0\frac{p}{Z}\left(1+\frac{\beta}{p}\right) \tag{12}$$

Using Eq. (8), the mass conservation Eq. (7) can be written in the following form:

$$C_f\frac{\partial p}{\partial t} + \nabla.\boldsymbol{q} = Q_s \tag{13}$$

where

187 $$C_f = \phi \frac{M_g}{R_g T Z}\left(1 - \frac{p}{Z}\frac{\partial Z}{\partial p}\right) + (1-\phi)\frac{\rho_s M_g}{V_{std}}\frac{V_L p_L}{(p_L + p)^2} \tag{14}$$

188 The derivative of the cubic Eq. (4) yields:

189 $$\frac{\partial Z}{\partial p} = \frac{1}{p}\frac{-BZ^2 - \left(A - 2B - 6B^2\right)Z + \left(2AB - 2B^2 - 3B^3\right)}{3Z^2 - 2(1-B)Z + \left(A - 2B - 3B^2\right)} \tag{15}$$

190 which gives:

191 $$C_f = \phi \frac{M_g}{R_g T Z}\left(1 + \frac{1}{Z}\frac{BZ^2 + \left(A - 2B - 6B^2\right)Z - \left(2AB - 2B^2 - 3B^3\right)}{3Z^2 - 2(1-B)Z + \left(A - 2B - 3B^2\right)}\right) + (1-\phi)\frac{\rho_s M_g}{V_{std}}\frac{V_L p_L}{(p_L + p)^2}$$

192 (16)

193 Thus, modeling compressible gas flow in low permeability formations using the fully implicit
194 scheme requires the simultaneous solution of the coupled Eq. (13) (in which we substitute Eq.
195 (16), Eq. (11) and Eq. (12)) and Eq. (4) (in which we substitute Eq. (5) and Eq. (6)). The
196 unknowns of this highly nonlinear coupled system of equations are the gas pressure p and
197 the compressibility factor Z.

198 # 3. The numerical model

199 An efficient numerical model is developed in this section to accurately solve the highly
200 nonlinear coupled equations of gas flow and EOS with slippage and adsorption. The model is
201 based on advanced spatial and temporal discretization methods. The lumped MFE method is
202 employed for the spatial discretization and the time discretization is performed with high-
203 order time integration methods via the MOL.

204 *3.1 Spatial discretization with the lumped MFE method*

With the lowest-order MFE method, the vector $\boldsymbol{q}$ inside each triangular element E is approximated with the linear Raviart-Thomas basis functions (see Younes et al. (2010) for details):

$$\boldsymbol{q} = \sum_{j=1}^{3} Q_j^E \boldsymbol{w}_j^E \tag{17}$$

where $Q_j^E = \int_{\partial E_j} \boldsymbol{q}.\boldsymbol{\eta}_j^{\boldsymbol{E}}$ is the mass flux across the edge ∂E_j of E, $\boldsymbol{\eta}_j^E$ is the outward unit normal vector to ∂E_j and $\boldsymbol{w}_j^E = \frac{1}{2|E|}\begin{pmatrix} x - x_j^E \\ y - y_j^E \end{pmatrix}$ is the Raviart-Thomas basis functions (Raviart and Thomas, 1977) with $\left(x_j^E, y_j^E\right)$ the coordinates of the node j faced to the edge ∂E_j of E and $|E|$ the area of E.

The variational formulation of Eq. (11) on the element E, using $\boldsymbol{w}_i^{\boldsymbol{E}}$ as test function writes

$$\int_E \left(K^{-1}\boldsymbol{q}\right).\boldsymbol{w}_i^{\boldsymbol{E}} = -\int_E \nabla p.\boldsymbol{w}_i^{\boldsymbol{E}} = \int_E p\nabla.\boldsymbol{w}_i^{\boldsymbol{E}} - \sum_j \int_{\partial E_j} p\boldsymbol{w}_i^{\boldsymbol{E}}.\boldsymbol{\eta}_j^{\boldsymbol{E}} \tag{18}$$

Using properties of $\boldsymbol{w}_i^{\boldsymbol{E}}$ (see Younes et al., 2010), Eq (18) simplifies to

$$\sum_j B_{i,j}^E Q_j^E = p_E - Tp_i^E \tag{19}$$

where $\boldsymbol{B}^E$ is the elemental matrix of terms $B_{i,j}^E = \int_E \left(K^{-1,E}\boldsymbol{w}_j^{\boldsymbol{E}}\right).\boldsymbol{w}_i^{\boldsymbol{E}}$, p_E is the mean pressure at the element E and Tp_i^E is the mean pressure at the edge ∂E_i.

Inverting Eq. (19) gives the mass flux Q_i^E as:

$$Q_i^E = \delta_i^E p_E - \sum_j B_{i,j}^{-1,E} Tp_j^E \tag{20}$$

where $\delta_i^E = \sum_j B_{i,j}^{-1,E}$.

With the lumped formulation of the MFE method (see Younes e*t al.*, 2006), the stationary and accumulation parts of the flux are distinguished and the storage term is associated to the edge as:

$$Q_i^E = \overline{Q}_i^E + Q_{s,i}^E - \lambda_i^E \frac{\partial Tp_i^E}{\partial t} \tag{21}$$

where $Q_{s,i}^E = \frac{1}{ne}\int_E Q_s$ is the sink/source term associated to the edge ∂E_i of the element E with ne the number of edges of E ($ne = 3$ for a triangular element), $\lambda_i^E = \frac{|E|}{ne} C_f\left(p_E, Z_E\right)$ is the compressibility coefficient associated to ∂E_i and $\overline{Q}_i^E$ is the steady state mass flux given by (see Younes *et al*., 2006):

$$\overline{Q}_i^E = \sum_j \left(\frac{\delta_i^E \delta_j^E}{\delta^E} - B_{i,j}^{-1,E} \right) Tp_j^E \tag{22}$$

where $\delta^E = \sum_i \delta_i^E$.

Using the continuity of the trace of pressure $\left(Tp_i = Tp_i^E = Tp_i^{E'}\right)$ at the edge i between the two adjacent elements E and E', the continuity of the flux $\left(Q_i^E + Q_i^{E'} = 0\right)$ across i writes:

$$\left(\lambda_i^E + \lambda_i^{E'}\right)\frac{\partial Tp_i^E}{\partial t} + \sum_j \left(B_{i,j}^{-1,E} - \frac{\delta_i^E \delta_j^E}{\delta^E} \right) Tp_j^E + \sum_j \left(B_{i,j}^{-1,E'} - \frac{\delta_i^{E'} \delta_j^{E'}}{\delta^{E'}} \right) Tp_j^{E'} = Q_{s,i}^E + Q_{s,i}^{E'} \tag{23}$$

This equation is written for all the edges of the mesh, which gives the final system to solve. Notice that the obtained system is highly nonlinear since the coefficients $K^E = K\left(Z_E, p_E\right)$, $B_{i,j}^{-1,E} = B_{i,j}^{-1,E}\left(Z_E, p_E\right)$, $\lambda_i^E = \lambda_i^E\left(Z_E, p_E\right)$, $\delta_j^E = \delta_j^E\left(Z_E, p_E\right)$ and $\delta^E = \delta^E\left(Z_E, p_E\right)$ are dependent on the sought pressure p_E and factor Z_E.

It is known that time solvers can ensure accurate and stable evolution of the solution in time for ODE systems, while some difficulties can be encountered for the solution of DAE systems

as the iteration matrix for DEA can be ill-conditioned when the time step is reduced (Brenan *et al*., 1996). To overcome these difficulties, a small transient term is added to the nonlinear algebraic cubic Peng-Robinson EOS to converted it to an ordinary differential equation. The added transient term is negligible in the PDE since it is multiplied by a very small factitious storage coefficient. The obtained transient Peng-Robinson EOS on the element E writes

$$s_E \frac{dZ_E}{dt} + Z_E^3 - (1-B) Z_E^2 + \left(A - 2B - 3B^2\right) Z_E - \left(AB - B^2 - B^3\right) = 0 \tag{24}$$

where the parameters $A(p_E)$ and $B(p_E)$ of the cubic equation are functions of the gas pressure p_E (see Eq. (5)) and s_E is a very small fictitious $\left(s_E \approx 10^{-10}\right)$ storage coefficient used to enhance the convergence of the ODE time solver.

3.2 Time discretization with high-order integration methods

With the MOL, all the spatial derivatives are discretized, while the time derivatives remain continuous (see Eq. (23) and Eq (24)). Subsequently, time integration is performed using high-order methods which allow larger time steps and less effort in the nonlinear solver compared to the low-order methods (Farthing et al., 2002). In addition, high-order methods are often combined with efficient time-stepping schemes where the time-step size is optimized in order to reduce the computational cost while maintaining a given temporal discretization error.

The equations (23)-(24) on all elements E are gathered into a single implicit system of ordinary differential equations (ODEs) of the general form

$$F\left(t, \boldsymbol{y}, \boldsymbol{y}'\right) = 0 \tag{25}$$

where $\boldsymbol{y} = \left[\left(Tp_i\right)_{i=1,..,nb\_edges}, \left(Z_E\right)_{E=1,..,nb\_elements} \right]$ is the vector of unknowns formed by: (*i*) the pressure traces at all the edges of the mesh (except boundary edges with prescribed pressure),

and (*ii*) the Z-factor at all the elements and $\boldsymbol{y}' = \left[\left(\partial Tp_i / \partial t \right)_{i=1,..,nb\_edges}, \left(\partial Z_E / \partial t \right)_{E=1,..,nb\_elements} \right]$. Thus, the number of unknowns is approximately the number of edges plus the number of elements.

The system (25) is integrated in time with the DASPK time solver (Brown et al., 1994). DASPK uses a variable order (up to five) time integration method based on the Fixed Leading Coefficient Backward Difference Formulas (FLCBDF) which has good stability properties. The *k*th-order FLCBDF method transforms the system $F\left(t_n, \boldsymbol{y}_n, \boldsymbol{y}'_n\right) = 0$ at the time $t_n = t_{n-1} + \underline{h}$ with the solution history $\boldsymbol{y}_{n-1}, ..., \boldsymbol{y}_{n-k}$ to a nonlinear system $F\left(t_n, \boldsymbol{y}_n, \hat{\boldsymbol{a}}\boldsymbol{y}_n + \hat{\boldsymbol{b}}\right) = 0$ where $\hat{\boldsymbol{a}}$ and $\hat{\boldsymbol{b}}$ depend on the order k, the step size $\underline{h}$, and the solution history (Brenan et al., 1996). The obtained nonlinear system is then solved with the Newton method using finite difference approximation of the Jacobian matrix $\boldsymbol{J}$. To improve efficiency, the same Jacobian is used over as many time steps as possible and is updated only when the nonlinear solver fails during time stepping. Further, the terms of $\boldsymbol{J}$ are calculated using the column grouping technique. This technique allows perturbing variables by group, knowing the structure of $\boldsymbol{J}$, which can be deduced from the Eqs (23) and (24). The obtained linear systems can be solved with either iterative or direct methods. In this work, we choose the preconditioned Krylov iterative method which is more adapted for large linear systems.

During simulation, both the order of the time integration and the time step size are optimized in order to minimize the computational effort while keeping both relative and absolute time errors under a small tolerance, fixed to 10^{-7} for all the simulations in this work.

4. Numerical experiments

4.1 Gas extraction in a heterogenous domain

In this section, numerical simulations of compressible gas flow with slippage and adsorption in a heterogeneous two-dimensional domain is performed to investigate the performance of the new model. All the simulations are carried out on an Intel Xeno E-2246G, CPU 3.60 GHz PC with 32.00 GB of RAM.

We consider an isothermal compressible gas flow, where the gas is methane, in a square $600m \times 600m$ heterogeneous domain. The domain is discretized with an unstructured mesh formed by 9858 triangular elements (Figure 1). The west and east boundaries have fixed pressures with, respectively, p_w and p_e. Both the north and south boundaries are impermeable. The domain has an intrinsic permeability k_1 and involves 6 rectangular heterogeneities having a smaller permeability $k_2 = k_1/1000$.

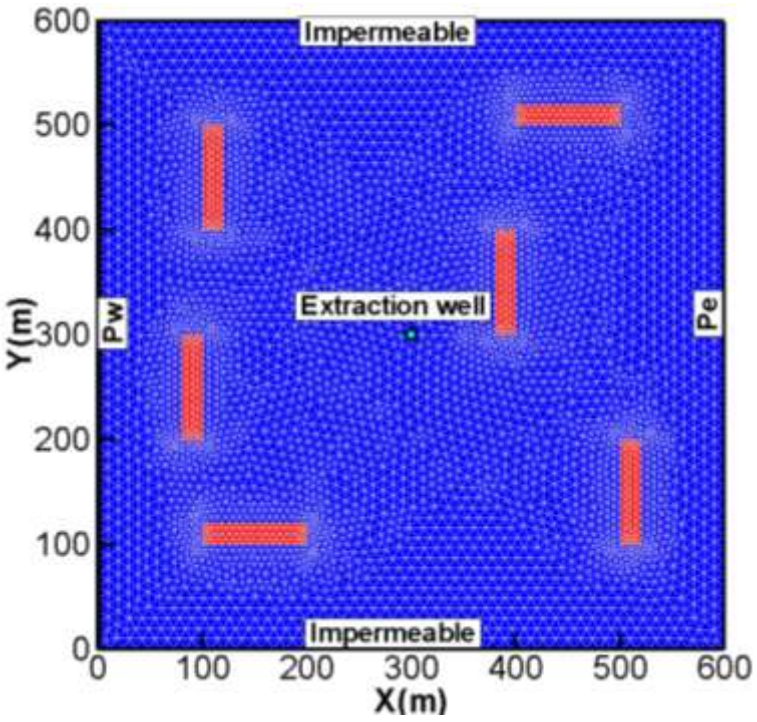

Figure 1: Permeability distribution and boundary conditions for the problem of gas extraction in a heterogenous domain (blue: permeability k_1; red: permeability $k_2 = k_1/1000$)

An extraction well is located at the center of the domain $(x_c = 300m, y_c = 300m)$. The pressure in the extraction well is fixed to p_{well}. The initial pressure in the domain is p_{init} and

300 the simulation time is set as 10^{11} s. The parameters for the numerical simulation are depicted
301 in Table 1.

302 **Table 1:** Parameters for the problem of gas extraction in a heterogenous domain.

Parameter	Value	Parameter	Value
ϕ (-)	0.05	V_L (m^3/mol)	2.83×10^{-3}
p_{init} (Pa)	10^7	ρ_s (kg/m^3)	2550
p_e (Pa)	10^7	V_{std} (m^3/mol)	0.0224
p_w (Pa)	10^8	T_c (K)	191
p_{well} (Pa)	4×10^6	T (K)	314
k_1 (m^2)	10^{-18}	p_L (Pa)	2.07×10^3
k_2 (m^2)	10^{-21}	p_c (Pa)	4.6×10^6
R_g (J/(mol K))	8.314	μ (Pa.s)	10^{-5}
ω (-)	0.011	β (Pa)	7×10^5
M_g (kg/mol)	0.016		

303

304 Figure 2 shows the final pressure distribution as well as the velocity field and streamlines
305 calculated with the new code. In this figure, a regional gas flow occurs from the west
306 boundary (high prescribed pressure) to the east boundary (lower prescribed pressure). The
307 extraction well creates a catchment area at the center of the domain and almost all extracted
308 gas is originated from the west boundary. The streamlines in Figure 2 show that the local
309 heterogeneities (with very low permeability) are circumvented by the gas flow. The evolution
310 of the cumulative extracted mass of gas during time is plotted in the Figure 3. The cumulative
311 mass of gas shows an almost linear evolution with time.
312 To investigate the effect of the factitious storage coefficient used to convert the nonlinear
313 algebraic cubic Peng-Robinson EOS to an ordinary differential equation, three simulations are
314 conducted using different small storage coefficients corresponding to 10^{-8}, 10^{-10} and 10^{-12}.
315 The three coefficients yield exactly the same results. The required CPU time for the three

316 simulations is respectively 6.9s, 7.5s and 7.9s. The increase of the CPU time, observed when
317 the factitious storage coefficient decreases, is mainly due to a larger number of evaluations of
318 the Jacobian matrix and smaller time step sizes at the beginning of the simulation. Notice that
319 the DASPK time solver encountered several convergence issues for $s_E \leq 10^{-16}$.
320 To show the benefit of using high order time integration methods, the studied problem is
321 simulated using two options: MOL_1 where the time integration is based on a first-order time
322 discretization method and MOL_V where the time integration is performed using variable
323 order method. The order of the time integration in MOL_V is adapted between 1 and 5 during
324 the simulation in order to maximize the time step size while keeping the temporal error small.
325 Results of simulations show that MOL_1 and MOL_V yield exactly the same solution in
326 terms of pressure distribution and extracted mass of gas. Figure 4 shows the evolution of the
327 time step size during the simulation with both MOL_1 (Figure 4a) and MOL_V (Figure 4b).
328 Both methods start with a very small time step, however, with MOL_V, the time step size
329 increases more rapidly than with MOL_1. Table 2 shows that MOL_1 requires 14815 time
330 steps for the entire simulation, whereas, MOL_V requires only 597 time steps. As a
331 consequence, MOL_V requires around 25 times less residual evaluations than MOL_1.
332 Furthermore, MOL_V requires less Jacobian evaluations than MOL_1. The mean time step
333 with MOL_V is 26 times greater than that with MOL_1. The entire simulation with MOL_1
334 requires 75s of CPU time, whereas, it needs only 7.4s with MOL_V. Thus the MOL_V
335 model, based on high order methods, is around 10 times more efficient than the MOL_1
336 model, which is based on the first order time integration method. This highlights the benefit of
337 using high order time integration methods for the solution of the nonlinear system of
338 equations governing compressible flow in low permeability formations with slippage and
339 nonlinear adsorption.
340

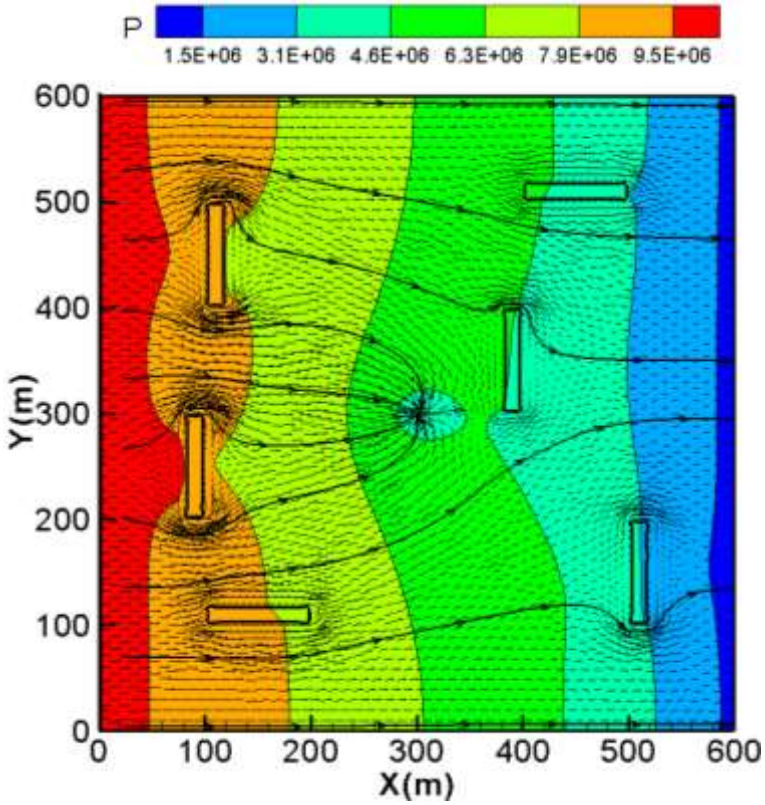

341

342 **Figure 2:** Pressure distribution, streamlines and velocity field for the problem of gas

343 extraction in a heterogenous domain.

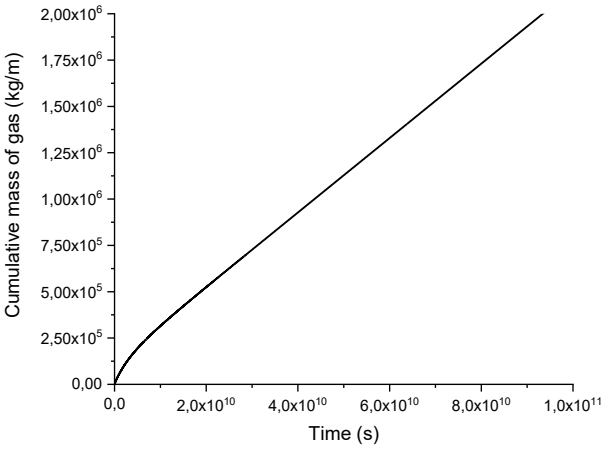

344

345 **Figure 3:** Cumulative mass of extracted gas.

346

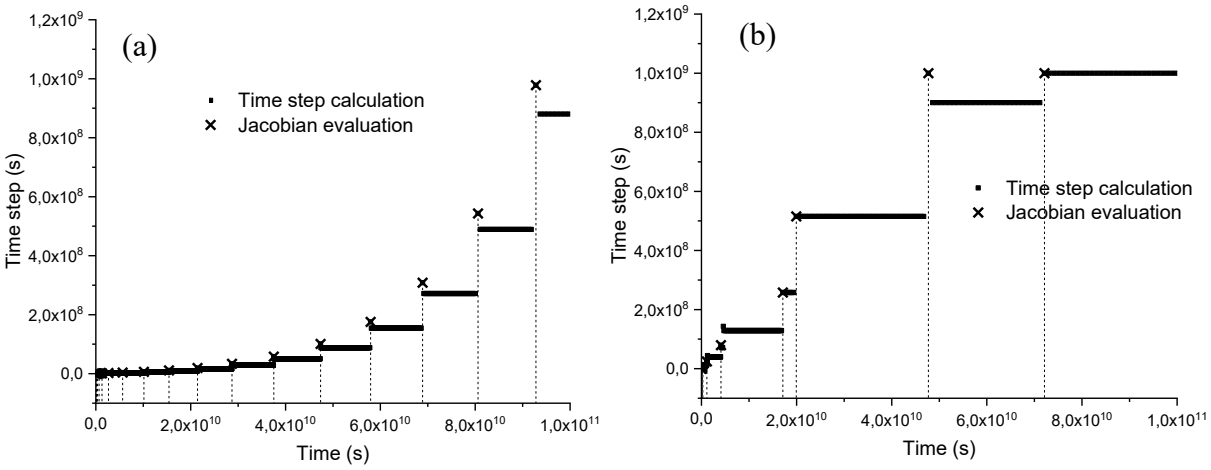

Figure 4: Time step evolution with MOl_1 (a) based on first order and MOL_V (b) based on variable order time integration methods.

	Nbr of residual evaluations	Nbr of Jacobian evaluations	Mean Δt	CPU
MOL_1	14815	43	6.8×10^{6} s	75 s
MOL_V	597	35	1.8×10^{8} s	7.4 s

Table 2: Comparison between first order and high-order time integration methods.

4.2 Influential parameters controlling the gas extraction rate

Accurate and efficient simulators are often necessary when several simulations are required, as for instance for Bayesian parameter estimation, global sensitivity or uncertainty analysis. In this section, Global Sensitivity Analysis (GSA) combined with the Polynomial Chaos Expansion (PCE) surrogate modelling is conducted to assess the influence of hydraulic parameters on the pumping rate of the gas extraction well. The test case is similar to the previous problem, but a homogeneous domain is considered with an initial gas pressure of 10^5 Pa and uniform boundary conditions with a prescribed gas pressure of 10^5 Pa at the four

boundaries of the square domain. The well pressure is fixed to 4×10^3 Pa. The rest of the parameters are similar to the previous test problem given in Table 1.

The numerical model is employed to analyze the uncertainty of the pumping rate of the gas extraction well associated with the following parameters: the intrinsic gas-phase permeability k_0, the Klinkenberg factor β, the Langmuir gas volume V_L, the Langmuir gas pressure p_L and the porosity ϕ. Sufficiently large uncertainty ranges are chosen (Table 3) to explore the role of each parameter. All parameters are assumed to be independent.

Table 3: Uncertainty ranges of parameters.

Parameter	Uncertainty Range
ϕ (-)	$[0.02, 0.1]$
k_0 (m^2)	$[10^{-18}, 10^{-17}]$
β (Pa)	$[10^5, 10^6]$
p_L (Pa)	$[0.5\times10^6, 15\times10^6]$
V_L (m^3/kg)	$[0.5\times10^{-3}, 10\times10^{-3}]$

The effect of the five parameters on the pumping rate is investigated using the Sobol variance-based sensitivity indices (Sobol, 2001). These indices measure the contribution of a parameter (alone or by interactions with other parameters) to the output (pumping rate) variance. The Sobol indices do not require any assumption of linearity or monotony of the model and are therefore, well suited for GSA. Two Sobol indices are generally calculated:

- the first-order (main effect) index,

$$S_i = \frac{V\left[E\left[y|\chi_i\right]\right]}{V\left[y\right]} = \frac{V_i}{V} \tag{26}$$

- the total index,

$$ST_i = \frac{V\left[E\left[y|\boldsymbol{\chi}_{-i}\right]\right]}{V\left[y\right]} = \frac{V_i^T}{V} \tag{27}$$

where y is the model output, $\boldsymbol{\chi}$ is the set of parameters $\boldsymbol{\chi} = (\phi, k_0, \beta, p_L, V_L)$, $E[\ ]$ is the average, $V[\ ]$ is the variance, $E[\ |\ ]$ and $V[\ |\ ]$ are their respective conditional forms. χ_i represents one of the parameters, and $\boldsymbol{\chi}_{-i}$ stands for all parameters $\boldsymbol{\chi}$, except the parameter χ_i.

The first-order index $S_i \in [0,1]$ quantifies the share of variance in y due to the parameter χ_i alone. The total sensitivity index $ST_i \in [0,1]$ measures the contribution of χ_i to the variance of y, including its interactions with the other parameters (i.e., $\boldsymbol{\chi}_{-i}$). If $S_i = ST_i$, then interactions between parameters are negligible.

In this work, the Sobol' indices are calculated using the Polynomial Chaos Expansion (PCE) surrogate modeling (Fajraoui et al., 2012; Shao et al., 2017; Younes et al., 2016). A full surrogate chaos polynomial of order 4 is constructed for the expansion with the five parameters. The number of polynomial coefficients is $\frac{9!}{5! \times 4!} = 126$. The coefficients are calculated by minimizing the sum of squared errors between the PCE and the model output. To this aim, 300 simulations are performed using parameter values randomly generated in the intervals of variation given in Table 3.

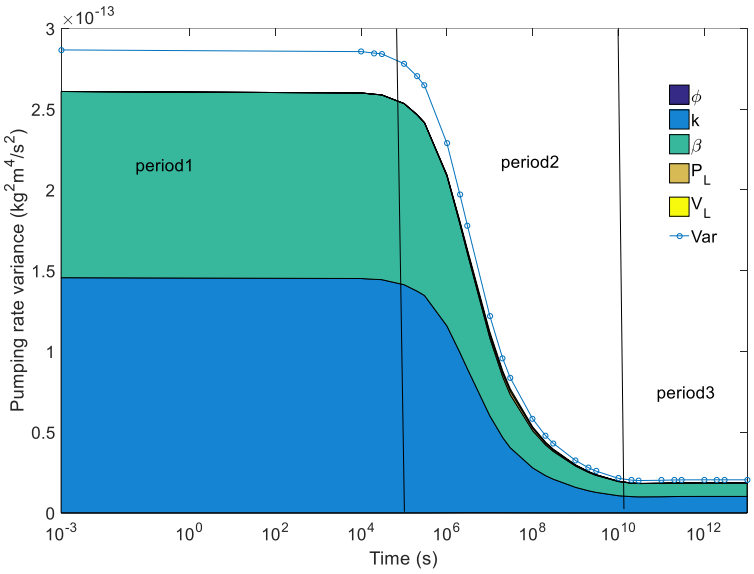

394

395 **Figure 5**: Pumping rate variance. The shaded areas represent the partial variance of each
396 parameter. The blank region below the variance curve and above the shaded areas represents
397 interactions between parameters.

398 Figure 5 depicts the pumping rate variance versus time. In this figure, the shaded areas
399 represent the amount of variance due to each parameter alone. The interaction between
400 parameters is represented by the blank region below the variance curve and above the shaded
401 area. In this figure, three periods can be distinguished. In the first short period $\left(t \le 10^5 s\right)$, the
402 variance of the pumping rate is constant (Figure 5). Because of the compressibility of the gas,
403 the mean pressure near the well and the mean pumping rate are constant (Figure 6). During
404 this period, only the parameters k_0 and β are influential with a small interaction between
405 them. The parameters ϕ, p_L and V_L are non-influential since their total sensitivity indices are
406 less than 10^{-4} (Table 4).

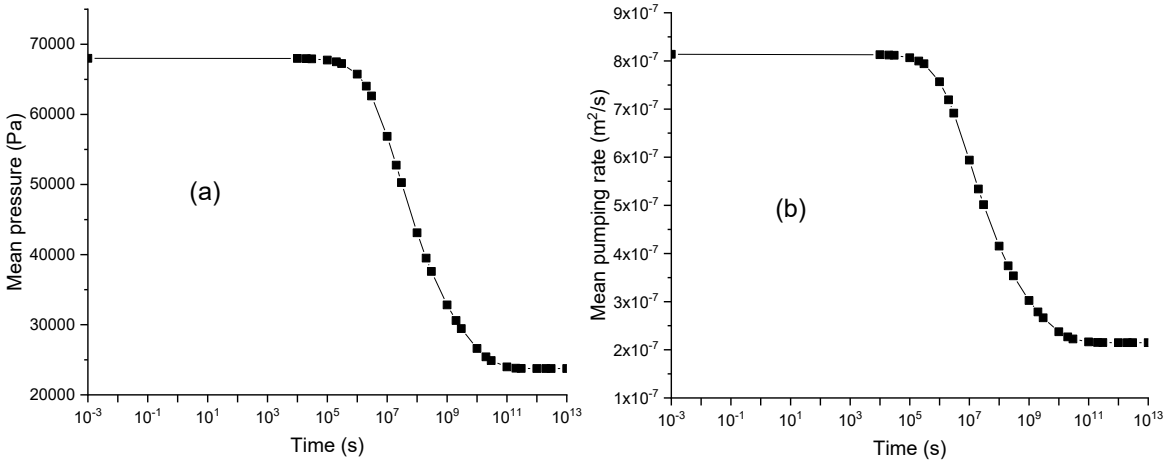

407

408 **Figure 6**: Evolution of the mean pressure near the well (a) and the mean pumping rate at the

409 well (b) during time.

410

	ϕ	k_0	β	p_L	V_L
	Period1 $\left(t = 10^5 s\right)$				
ST_i	0	0.6	0.5	0	0
S_i	0	0.5	0.4	0	0
	Period2 $\left(t = 2 \times 10^7 s\right)$				
ST_i	0	0.56	0.46	0.04	0.03
S_i	0	0.49	0.39	0.02	0.02
	Period3 $\left(t = 10^{12} s\right)$				
ST_i	0	0.59	0.5	0	0
S_i	0	0.5	0.4	0	0

411

412 **Table 4**: Total and first order Sobol indices of the hydraulic parameters for the three periods.

413 In the second period $\left(10^5 s \le t \le 10^{10} s\right)$, the depression created by the well propagates in the

414 domain and the capture zone increases with time. As a consequence, the pressure near the

415 well decreases and also the mean flow rate (Figure 6). During this period the most influential

416 parameters remain k_0 and then β. The porosity has no effect on the pumping rate $\left(ST_i = 0\right)$.

417 A small effect is observed for p_L $\left(ST_i = 0.04\right)$ and V_L $\left(ST_i = 0.03\right)$. To investigate how each

418 parameter affects the pumping rate, the PCE is used to calculate the marginal effect of each

parameter on the model output. This effect is obtained by analyzing the variation of the model output with respect to the chosen parameter whereas the other parameters are fixed at their mean values. The marginal effects of the parameters are shown in the Figure 7. Figure 7a shows that the pumping rate has an almost constant value whatever the value of the porosity. Figures 7b and 7c show that the two parameters k_0 and β have a strong effect on the pumping rate with an almost linear increase of the pumping rate when k_0 or β increases. Figure 7d shows that the pumping rate is weakly influenced by p_L. When the parameter p_L increases, a weak decrease of the pumping rate is observed. Note that the effect of p_L on the pumping rate is not uniform. Indeed, the slope of the curve in the Figure 7d is more significant (which reflects a higher sensitivity) for low p_L values $\left(\leq 10^6 Pa\right)$ than for higher values $\left(>10^6 Pa\right)$, for which the pumping rate is almost constant. Finally, Figure 7e shows a small increase of the pumping rate when V_L increases, which explains the very weak sensitivity of the pumping rate to V_L.

The last period $\left(10^{10} s \leq t\right)$ corresponds to the steady state regime in the whole domain where no evolution of the pressure distribution occurs. The pumping rate reaches its minimum value and all the extracted gas is originated from the boundaries of the domain. In this period, only the parameters k_0 and β are influential, as in period1.

In summary, the main parameters controlling the pumping rate of the gas extraction well during the whole simulation are the intrinsic gas permeability k_0 and the slippage factor β.

The results of this test case demonstrate the applicability of the developed model for an efficient solution of compressible flow in low permeability formations with slippage and nonlinear adsorption, in the context of global sensitivity analysis.

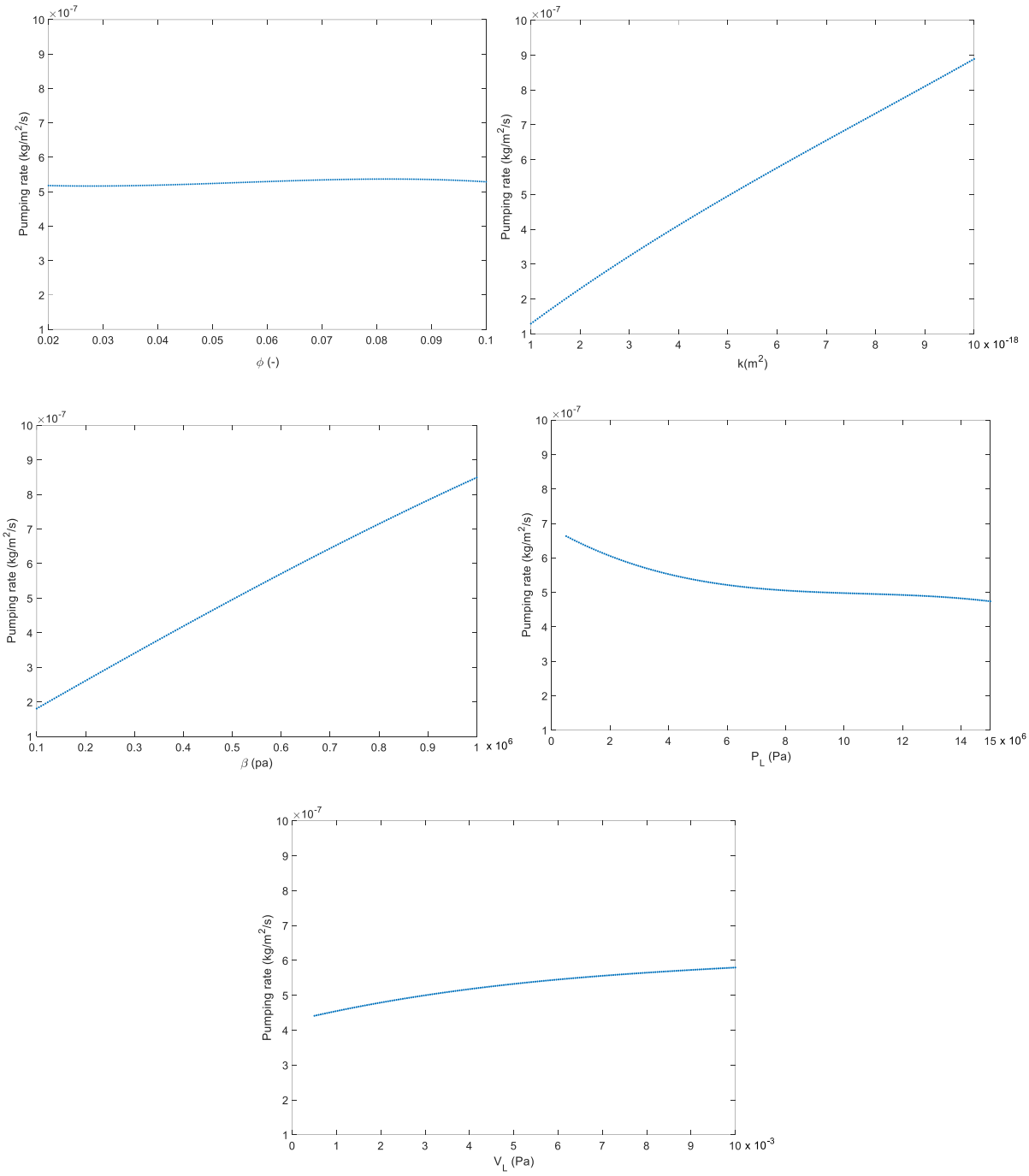

Figure 7: Marginal effects of ϕ, k, β, p_L, V_L on the pumping rate of the gas extraction well at period2 $\left(t = 2\times10^7 s\right)$.

5. Conclusion

Simulation of gas flow in low permeability formations can be computationally demanding because of the high nonlinearities induced by the compressibility of the gas, the slippage effect and the nonlinear adsorption of gas on the pore surface. In this work, an efficient model is developed using advanced spatial and temporal discretization methods for a simultaneous solution of the gas flow equation and the cubic Peng-Robinson EOS with Klinkenberg slippage effect and Langmuir adsorption. The spatial discretization is based on the MFE method which is well adapted for heterogeneous porous media and unstructured meshes. The lumped hybrid formulation of the MFE method is used since it improves the monotonicity of the scheme and allows the use of the MOL. Time discretization is performed with high-order time integration methods. The time step size and the order of the time integration are optimized during the simulation in order to reduce the computational cost while maintaining a given temporal discretization error.

The developed model is used for the simulation of gas extraction in a heterogeneous domain. The results of this test case show that the cumulative extracted mass of gas has an almost linear evolution with time. Both first-order and high-order time discretization methods yield the same results, however, the time step size increases more rapidly with the high-order method and allows a reduction by a factor of 10 in the computational time as compared to the first-order method. This highlights the benefit of using high order time integration methods for the solution of gas flow in low permeability formations.

The new model is then employed to assess the influence of hydraulic parameters on the pumping rate of the gas extraction well in the case of a homogeneous aquifer. The GSA is performed using PCE surrogate modeling. The efficient simulator developed in this work is suited to perform GSA since several simulations are required to assess the sensitivity indices. The results of this test case show that the main hydraulic parameters controlling the well

475 pumping rate for the investigated test case are the intrinsic gas permeability and the slippage
476 factor.
477 The 2D formulation developed in this work is quite generic and can be easily extended to 3D
478 problems without too much complicated numerical developments.
479
480

References

Baehr, A.L., Hult, M.F., 1991. Evaluation of Unsaturated Zone Air Permeability Through Pneumatic Tests. Water Resour. Res. 27, 2605–2617. https://doi.org/10.1029/91WR01655

Baniasadi, Maryam, Mohebbi, A., Baniasadi, Mehdi, 2012. A new correlation based on artificial neural networks for predicting the natural gas compressibility factor. J. Eng. Thermophys. 21, 248–258. https://doi.org/10.1134/S1810232812040030

Bastian, P., Helmig, R., 1999. Efficient fully-coupled solution techniques for two-phase flow in porous media: Parallel multigrid solution and large scale computations. Adv. Water Resour. 23, 199–216. https://doi.org/10.1016/S0309-1708(99)00014-7

Brenan, K.E., Campbell, S.L., Petzold, L.R., 1996. Numerical Solution of Initial-value Problems in Differential-algebraic Equations. SIAM, New York. https://doi.org/10.1137/1.9781611971224

Brezzi, F., Fortin, M., 1991. Mixed and hybrid finite element methods, Springer series in computational mathematics. Springer, New York Berlin Heidelberg. https://doi.org/10.1007/978-1-4612-3172-1

Brown, P.N., Hindmarsh, A.C., Petzold, L.R., 1994. Using Krylov Methods in the Solution of Large-Scale Differential-Algebraic Systems. SIAM J. Sci. Comput. 15, 1467–1488. https://doi.org/10.1137/0915088

Chamkalani, A., Mae'soumi, A., Sameni, A., 2013. An intelligent approach for optimal prediction of gas deviation factor using particle swarm optimization and genetic algorithm. J. Nat. Gas Sci. Eng. 14, 132–143. https://doi.org/10.1016/j.jngse.2013.06.002

Chavent, G., Jaffré, J., 1986. Mathematical models and finite elements for reservoir simulation: single phase, multiphase, and multicomponent flows through porous media, Studies in mathematics and its applications. Elsevier Science Pub, New York, U.S.A.

Chavent, G., Roberts, J.E., 1991. A unified physical presentation of mixed, mixed-hybrid finite elements and standard finite difference approximations for the determination of velocities in waterflow problems. Adv. Water Resour. 14, 329–348. https://doi.org/10.1016/0309-1708(91)90020-O

Civan, F., Rai, C.S., Sondergeld, C.H., 2011. Shale-Gas Permeability and Diffusivity Inferred by Improved Formulation of Relevant Retention and Transport Mechanisms. Transp. Porous Media 86, 925–944. https://doi.org/10.1007/s11242-010-9665-x

Cui, X., Bustin, A.M.M., Bustin, R.M., 2009. Measurements of gas permeability and diffusivity of tight reservoir rocks: different approaches and their applications. Geofluids 9, 208–223. https://doi.org/10.1111/j.1468-8123.2009.00244.x

El Amin, M., Kou, J., Sun, S., 2018. Mixed Finite Element Simulation with Stability Analysis for Gas Transport in Low-Permeability Reservoirs. Energies 11, 208. https://doi.org/10.3390/en11010208

El Amin, M.F., Amir, S., Salama, A., Urozayev, D., Sun, S., 2017. Comparative study of shale-gas production using single- and dual-continuum approaches. J. Pet. Sci. Eng. 157, 894–905. https://doi.org/10.1016/j.petrol.2017.07.011

Elliott, J., Lira, C., 2012. Introductory Chemical Engineering Thermodynamics, 2nd ed. Prentice Hall, New York.

Essaid, H.I., Bekins, B.A., Cozzarelli, I.M., 2015. Organic contaminant transport and fate in the subsurface: Evolution of knowledge and understanding. Water Resour. Res. 51, 4861–4902. https://doi.org/10.1002/2015WR017121

Fajraoui, N., Mara, T.A., Younes, A., Bouhlila, R., 2012. Reactive Transport Parameter Estimation and Global Sensitivity Analysis Using Sparse Polynomial Chaos Expansion. Water. Air. Soil Pollut. 223, 4183–4197. https://doi.org/10.1007/s11270-012-1183-8

Farthing, M.W., Kees, C.E., Miller, C.T., 2002. Mixed finite element methods and higher-order temporal approximations. Adv. Water Resour. 25, 85–101. https://doi.org/10.1016/S0309-1708(01)00022-7

Foo, K.Y., Hameed, B.H., 2010. Insights into the modeling of adsorption isotherm systems. Chem. Eng. J. 156, 2–10. https://doi.org/10.1016/j.cej.2009.09.013

Hughes, T.J., Honari, A., Graham, B.F., Chauhan, A.S., Johns, M.L., May, E.F., 2012. CO2 sequestration for enhanced gas recovery: New measurements of supercritical CO2–CH4 dispersion in porous media and a review of recent research. Int. J. Greenh. Gas Control 9, 457–468. https://doi.org/10.1016/j.ijggc.2012.05.011

Huyakorn, P.S., Panday, S., Wu, Y.S., 1994. A three-dimensional multiphase flow model for assesing NAPL contamination in porous and fractured media, 1. Formulation. J. Contam. Hydrol. 16, 109–130. https://doi.org/10.1016/0169-7722(94)90048-5

Jia, B., Li, D., Tsau, J.-S., Barati, R., 2017. Gas Permeability Evolution During Production in the Marcellus and Eagle Ford Shales: Coupling Diffusion/Slip-flow, Geomechanics, and Adsorption/Desorption. Presented at the SPE/AAPG/SEG Unconventional Resources Technology Conference, OnePetro. https://doi.org/10.15530/URTEC-2017-2695702

Jones, S.C., 1972. A Rapid Accurate Unsteady-State Klinkenberg Permeameter. Soc. Pet. Eng. J. 12, 383–397. https://doi.org/10.2118/3535-PA

Klinkenberg, L.J., 1941. The permeability of porous media to liquids and gases. Drill. Prod. Pract. 200–213.

Koohbor, B., Fahs, M., Hoteit, H., Doummar, J., Younes, A., Belfort, B., 2020. An advanced discrete fracture model for variably saturated flow in fractured porous media. Adv. Water Resour. 140, 103602. https://doi.org/10.1016/j.advwatres.2020.103602

Li, J., Fan, X., Wang, Y., Yu, B., Sun, S., Sun, D., 2020. A POD-DEIM reduced model for compressible gas reservoir flow based on the Peng-Robinson equation of state. J. Nat. Gas Sci. Eng. 79, 103367. https://doi.org/10.1016/j.jngse.2020.103367

Lopez-Echeverry, J.S., S. Reif-Acherman, E. Araujo-Lopez, Peng-Robinson equation of state: 40 years through cubics, Fluid Phase Equilib. 447 (2017),39–71, https://doi.org/10.1016/j.fluid.2017.05.007.

Mahmoud, M. (2014). Development of a new correlation of gas compressibility factor (Z-factor) for high pressure gas reservoirs. J. Energy Resour. Technol., 136(1), https://doi.org/10.2118/164587-MS

Moiseeva, E.F., Malyshev, V.L., 2019. Compressibility factor of natural gas determination by means of molecular dynamics simulations. AIP Adv. 9, 055108. https://doi.org/10.1063/1.5096618

Peng, D.-Y., Robinson, D.B., 1976. A New Two-Constant Equation of State. Ind. Eng. Chem. Fundam. 15, 59–64. https://doi.org/10.1021/i160057a011

Pruess, K., 1991. TOUGH2: A general-purpose numerical simulator for multiphase fluid and heat flow. p. LBL-29400, 5212064. https://doi.org/10.2172/5212064

Raviart, P.A., Thomas, J.M., 1977. A mixed finite element method for 2-nd order elliptic problems, in: Galligani, I., Magenes, E. (Eds.), Mathematical Aspects of Finite Element Methods, Lecture Notes in Mathematics. Springer, Berlin, Heidelberg, pp. 292–315. https://doi.org/10.1007/BFb0064470

Reda, D.C., 1987. Slip-Flow Experiments in Welded Tuff: The Knudsen Diffusion Problem. Elsevier, pp. 485–493. https://doi.org/10.1016/B978-0-12-701620-7.50039-8

579 Salama, A., Amin, M.F.E., Kumar, K., Sun, S., 2017. Flow and Transport in Tight and Shale
580 Formations: A Review. Geofluids 2017, 1–21. https://doi.org/10.1155/2017/4251209
581 Samuel, J.-S., Muggeridge, A.H., 2020. Fast Modelling of Gas Reservoirs Using POD-RBF
582 Non-Intrusive Reduced Order Modelling, in: Day 2 Wed, November 18, 2020.
583 Presented at the SPE Asia Pacific Oil & Gas Conference and Exhibition, SPE, Virtual,
584 p. D023S005R001. https://doi.org/10.2118/202436-MS
585 Shabro, V., Torres-Verdin, C., Javadpour, F., 2011. Numerical Simulation of Shale-Gas
586 Production: from Pore-Scale Modeling of Slip-Flow, Knudsen Diffusion, and
587 Langmuir Desorption to Reservoir Modeling of Compressible Fluid. Presented at the
588 North American Unconventional Gas Conference and Exhibition, OnePetro.
589 https://doi.org/10.2118/144355-MS
590 Shao, Q., Younes, A., Fahs, M., Mara, T.A., 2017. Bayesian sparse polynomial chaos
591 expansion for global sensitivity analysis. Comput. Methods Appl. Mech. Eng. 318,
592 474–496. https://doi.org/10.1016/j.cma.2017.01.033
593 Sobol, I.M., 2001. Global sensitivity indices for nonlinear mathematical models and their
594 Monte Carlo estimates. Math. Comput. Simul., The Second IMACS Seminar on
595 Monte Carlo Methods 55, 271–280. https://doi.org/10.1016/S0378-4754(00)00270-6
596 Wang, C.; Jia, A.; Guo, Z.; Huang, S.; Shi, X.; Cui, F. An Improved Correlation of
597 Compressibility Factor Prediction of Variable CO2-Content Condensate Gases.
598 Energies 2023, 16, 105. https://doi.org/10.3390/en16010105
599 Wang, J., Zhang, X., Bengough, A.G., Crawford, J.W., 2005. Domain-decomposition method
600 for parallel lattice Boltzmann simulation of incompressible flow in porous media.
601 Phys. Rev. E 72, 016706. https://doi.org/10.1103/PhysRevE.72.016706
602 Wilson, D.E., Montgomery, R.E., Sheller, M.R., 1987. A mathematical model for removing
603 volatile subsurface hydrocarbons by miscible displacement. Water. Air. Soil Pollut.
604 33, 231–255. https://doi.org/10.1007/BF00294194
605 Wu, Y.-S., Pruess, K., Persoff, peter, 1998. Gas Flow in Porous Media With Klinkenberg
606 Effects. Transp. Porous Media 32, 117–137.
607 https://doi.org/10.1023/A:1006535211684
608 Wu, Y.-S., Zhang, K., Ding, C., Pruess, K., Elmroth, E., Bodvarsson, G.S., 2002. An efficient
609 parallel-computing method for modeling nonisothermal multiphase flow and
610 multicomponent transport in porous and fractured media. Adv. Water Resour. 25,
611 243–261. https://doi.org/10.1016/S0309-1708(02)00006-4
612 Xiao, D., Lin, Z., Fang, F., Pain, C.C., Navon, I.M., Salinas, P., Muggeridge, A., 2017. Non-
613 intrusive reduced-order modeling for multiphase porous media flows using Smolyak
614 sparse grids. Int. J. Numer. Methods Fluids 83, 205–219.
615 https://doi.org/10.1002/fld.4263
616 Younes, A., Ackerer, P., Delay, F., 2010. Mixed finite elements for solving 2-D diffusion-
617 type equations. Rev. Geophys. 48. https://doi.org/10.1029/2008RG000277
618 Younes, A., Ackerer, P., Lehmann, F., 2006. A new mass lumping scheme for the mixed
619 hybrid finite element method. Int. J. Numer. Methods Eng. 67, 89–107.
620 https://doi.org/10.1002/nme.1628
621 Younes, A., Delay, F., Fajraoui, N., Fahs, M., Mara, T.A., 2016. Global sensitivity analysis
622 and Bayesian parameter inference for solute transport in porous media colonized by
623 biofilms. J. Contam. Hydrol. 191, 1–18. https://doi.org/10.1016/j.jconhyd.2016.04.007
624 Younes, A., Fahs, M., Ahmed, S., 2009. Solving density driven flow problems with efficient
625 spatial discretizations and higher-order time integration methods. Adv. Water Resour.
626 32, 340–352. https://doi.org/10.1016/j.advwatres.2008.11.003
627 Younes, A., Konz, M., Fahs, M., Zidane, A., Huggenberger, P., 2011. Modelling variable
628 density flow problems in heterogeneous porous media using the method of lines and

advanced spatial discretization methods. Math. Comput. Simul., MAMERN 2009: 3rd International Conference on Approximation Methods and Numerical Modeling in Environment and Natural Resources 81, 2346–2355. https://doi.org/10.1016/j.matcom.2011.02.010

Younes, A., Koohbor, B., Belfort, B., Ackerer, P., Doummar, J., Fahs, M., 2022. Modeling variable-density flow in saturated-unsaturated porous media: An advanced numerical model. Adv. Water Resour. 159, 104077. https://doi.org/10.1016/j.advwatres.2021.104077